COMPUTER METHODS IN BIOMECHANICS AND BIOMEDICAL ENGINEERING
2021, VOL. 24, NO. 2, 137–150
https://doi.org/10.1080/10255842.2020.1814755



# Muscle co-contraction in an upper limb musculoskeletal model: EMG-assisted vs. standard load-sharing

Ehsan Sarshari[a,b], Matteo Mancuso[c], Alexandre Terrier[b], Alain Farron[d], Philippe Mullhaupt[a] and Dominique Pioletti[b]

[a]Automatic Control Laboratory, Ecole Polytechnique Fédérale de Lausanne (EPFL), Lausanne, Switzerland; [b]Laboratory of Biomechanical Orthopedics, Ecole Polytechnique Fédérale de Lausanne (EPFL), Lausanne, Switzerland; [c]Laboratory of Movement Analysis and Measurement, Ecole Polytechnique Fédérale de Lausanne (EPFL), Lausanne, Switzerland; [d]Service of Orthopaedic Surgery and Traumatology, Lausanne University Hospital and University of Lausanne (CHUV), Lausanne, Switzerland

**ABSTRACT**

Estimation of muscle forces in over-actuated musculoskeletal models involves optimal distributions of net joint moments among muscles by a standard load-sharing scheme (SLS). Given that co-contractions of antagonistic muscles are counterproductive in the net joints moments, SLS might underestimate the co-contractions. Muscle co-contractions play crucial roles in stability of the glenohumeral (GH) joint. The aim of this study was to improve estimations of muscle co-contractions by incorporating electromyography (EMG) data into an upper limb musculoskeletal model. To this end, the model SLS was modified to develop an EMG-assisted load-sharing scheme (EALS). EMG of fifteen muscles were measured during arm flexion and abduction on a healthy subject and fed into the model. EALS was compared to SLS in terms of muscle forces, GH joint reaction force, and a stability ratio defined to quantify the GH joint stability. The results confirmed that EALS estimated higher muscle co-contractions compared to the SLS (e.g., above 50 N higher forces for both triceps long and biceps long during arm flexion).

**ARTICLE HISTORY**
Received 1 April 2019
Accepted 21 August 2020

**KEYWORDS**
Muscle over-actuations; inverse dynamics; muscle force estimations; antagonistic muscle co-contractions; Hill-type models

## 1. Introduction

Noninvasive measurement of muscle forces remains an elusive goal (Dennerlein 2005). However, estimations of these forces can be obtained using musculoskeletal models. In the available musculoskeletal models, equilibrium equations are obtained for net joint moments using inverse dynamics (Garner and Pandy 2001; Arnold et al. 2010; Ingram et al. 2016). There are more muscles than the number of equilibrium equations (over-actuation). Therefore, a standard load-sharing scheme (SLS) is used to distribute the net joint moments among muscles (Herzog 1996; Erdemir et al. 2007; Terrier et al. 2010). The SLS estimates muscle forces by optimizing a physiological cost function subject to constraints. The constraints are associated with the equilibrium equations, muscle force upper/lower bounds, and joint stability (Van der Helm 1994). Antagonistic muscles are counterproductive in the net joint moments. Therefore, SLS might underestimate forces produced by antagonistic muscles (co-contractions) (Cholewicki et al. 1995; Collins 1995; Gagnon et al. 2011; Engelhardt et al. 2015), consequently underestimating joint reaction forces (Favre et al. 2005; 2009; Nikooyan et al. 2012). Estimations of muscle and joint forces could be improved by considering co-contractions (Labriola et al. 2005; Yanagawa et al. 2008; Sarshari et al. 2017).

For the upper extremity, few studies investigated muscle co-contractions. Co-contractions were enforced either by tailoring the optimization of SLS (Van der Helm 1994; Raikova 1999; Forster et al. 2004) or by explicit use of measured EMG data (Laursen et al. 1998; Brookham et al. 2011; Nikooyan et al. 2012; Engelhardt et al. 2015).

Negative weighting factors were introduced to enforce co-contraction by alleviating the SLS cost function growth (Raikova 1999; Forster et al. 2004). The choice of weighting factors required *a priori* knowledge of antagonistic muscles. However, this was not straightforward to achieve, given that muscles could act simultaneously as agonistic and antagonistic. A stability constraint replicating the stabilizing and proprioceptive effects of musculotendinous structures was introduced for the GH joint (Van der Helm 1994; Garner and Pandy 2001; Ingram et al. 2016). It

CONTACT Ehsan Sarshari ehsan.sarshari@alumni.epfl.ch

constrained SLS solutions such that the resulting GH joint reaction force (JRF) always pointed toward the inside of the glenoid fossa.

On the other hand, explicit use of measured EMG data could provide rather straightforward estimations of co-contractions (Laursen et al. 1998; Brookham et al. 2011; Nikooyan et al. 2012; Engelhardt et al. 2015). The relationship between EMG data and muscle forces was crucial to ensure reliable EMG-based muscle force estimation. However, the EMG-force relationship was often over-simplified (Laursen et al. 1998; Brookham et al. 2011; Engelhardt et al. 2015) deviating from nonlinear dynamical behavior of musculotendon units (Zajac 1989). Besides, there was no guarantee that the net moments reproduced by EMG-based muscle forces would satisfy the equilibrium equations (Laursen et al. 1998; Langenderfer et al. 2005; Engelhardt et al. 2015). Therefore, the estimated co-contractions might lack a physiological correspondence. EMG-based muscle forces could shrink feasible sets of SLS. Therefore, co-contractions would be better estimated, if EMG data were measured for more muscles. EMG data were measured for fourteen muscles (Nikooyan et al. 2012), but only a subset of the measurements could be used simultaneously, otherwise "the model crashed".

The aim of this study was to improve estimations of muscle co-contractions by incorporating muscle EMG data into an upper limb musculoskeletal model. Three main improvements were considered with respect to the state-of-the-art. First, a validated nonlinear dynamical model was used for the EMG-force relationship. Second, the model SLS was modified to develop an EMG-assisted load-sharing (EALS) guarantying that the EMG-based forces would satisfy the equilibrium equations. Third, EMG data of fifteen muscles were measured on a healthy subject during arm flexion and abduction and simultaneously fed into the EALS. Muscle and joint force estimations by EALS were compared with those of the SLS.

## 2. Methods

EMG and motion data were measured (Section 2.1). A shoulder and elbow musculoskeletal model was developed (Section 2.2). The measured motions were reconstructed (Section 2.3). A musculotendon model was developed (Section 2.4). The EALS was detailed (Section 2.5). The developed EALS was evaluated and compared to the SLS (Section 2.6).

### 2.1. Measurements

EMG and motion data were recorded on a healthy male subject (29 year, 186 cm, and 85.5 kg) during forward flexion in the sagittal plane and abduction in the frontal plane, both with 2 kg weight in hand and with a fully extended elbow (Figure 1). Both activities were repeated for ten trials.

EMG signals of fifteen superficial muscles were measured at 1500 Hz sampling frequency using AgCl Kendall surface-button EMG electrodes and recorded by a 16 channel Desktop DTS system (Noraxon, Arizona, USA). The muscles were deltoid clavicular/acromial/scapular, trapezius C7/T1/T2-T7, pectoralis major sternal, infraspinatus, teres major, triceps brachii long/lateral, biceps brachii short/long, brachialis, and flexor carpi ulnaris. Maximum EMG values were also recorded by performing maximum voluntary contractions (MVC).

A common approach in the literature (Winter 2009; Hug 2011) was used in order to transform the measured EMG signals to muscle excitations. It consisted of high-pass filtering, rectifying, and consequently low-pass filtering the EMG signals. The resulting EMG signals were normalized for each muscle using the maximum of its associated MVC signal. Means and standard deviations ($\sigma_{EMG}$) of the

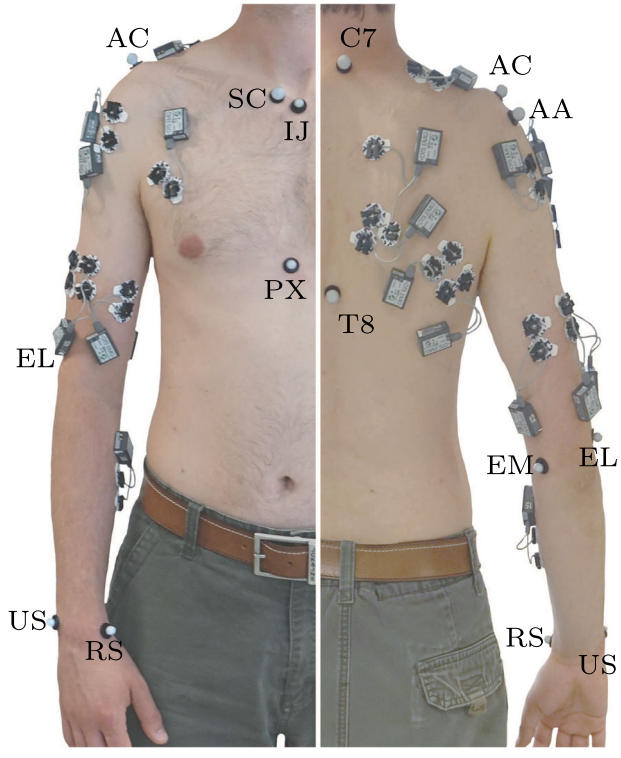


**Figure 1.** EMG data of fifteen superficial muscles and trajectories of eleven skin-fixed markers were recorded during arm flexion and extension with 2 kg weight in hand.

parted signals associating to the ten trials were obtained.

Trajectories of eleven palpable bony landmarks were measured by tracking their associated skin-fixed markers using an 8 camera VICON videogrammetry system (VICON, UK) at 100 Hz sampling frequency. The bony landmarks included incisura jugularis (IJ), processus xiphoideus (PX), 7th cervical vertebra (C7), 8th thoracic vertebra (T8), sternoclavicular (SC), acromioclavicular (AC), angulus acromialis (AA), medial epicondyle (EM), lateral epicondyle (EL), radial styloid (RS), and ulnar styloid (US).

The recorded trajectories were low-pass filtered. Then, means of the parted trajectories corresponding to the ten trials were obtained.

## 2.2. Upper extremity musculoskeletal model

### 2.2.1. Kinematic model

A shoulder and elbow musculoskeletal model was developed from MRI scans of the same subject (Figure 2(a)) (Ingram 2015; Ingram et al. 2016; Sarshari 2018). It consisted of six rigid bodies including thorax, clavicle, scapula, humerus, ulna,

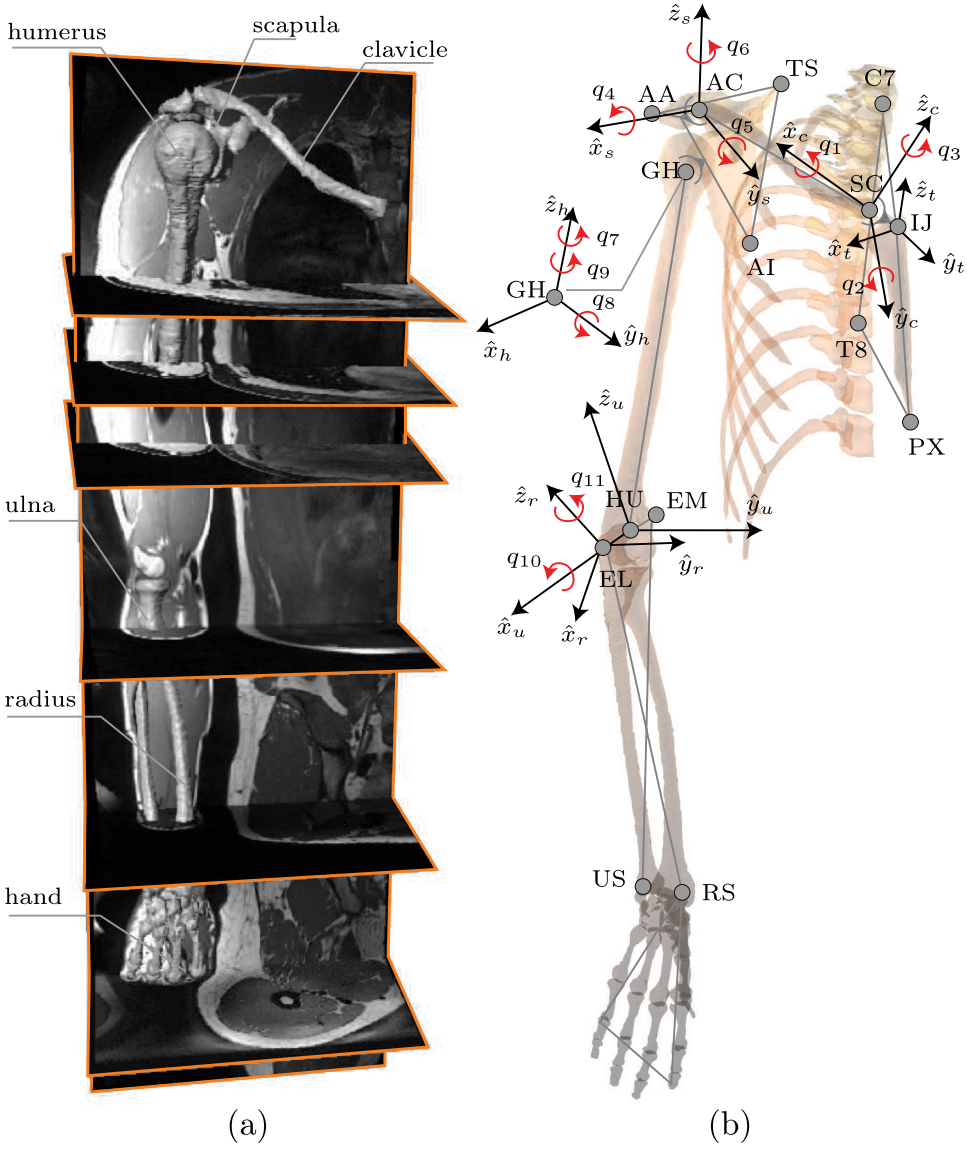


**Figure 2.** (a) MRI scans of a healthy subject were used to develop the model. (b) The kinematic model; fifteen bony landmarks were used, including IJ, PX, C7, T8, SC, AC, AA, TS, AI, GH, EM, EL, and the middle point of EM and EL (HU), RS, and US. The bone-fixed frames were: thorax frame $\{\boldsymbol{IJ}, \hat{x}_t, \hat{y}_t, \hat{z}_t\}$, clavicle frame $\{\boldsymbol{SC}, \hat{x}_c, \hat{y}_c, \hat{z}_c\}$, scapula frame $\{\boldsymbol{AC}, \hat{x}_s, \hat{y}_s, \hat{z}_s\}$, humerus frame $\{\boldsymbol{GH}, \hat{x}_h, \hat{y}_h, \hat{z}_h\}$, ulna frame $\{\boldsymbol{HU}, \hat{x}_u, \hat{y}_u, \hat{z}_u\}$, and radius frame $\{\boldsymbol{EL}, \hat{x}_r, \hat{y}_r, \hat{z}_r\}$. The generalized coordinates consisted of $q_1$: SC axial rotation, $q_2$: SC depression/elevation, $q_3$: SC protraction/retroaction, $q_4$: AC posterior/anterior tilt, $q_5$: AC downward/upward rotation, $q_6$: AC protraction/retroaction, $q_7$: GH axial rotation, $q_8$: GH addcution/abduction, $q_9$: GH flexion/extension, $q_{10}$: HU extension/flexion, $q_{11}$: RU pronation/supination. The humerus frame was shifted for better visualizations.

and radius. It had nine degrees of freedom (DOF) attributing to three ball-and-socket joints associating with sternoclavicular (SC), acromioclavicular (AC), and glenohumeral (GH) joints and two hinge joints for humeroulnar (HU) and radioulnar (RU) joints and two holonomic constraints (Figure 2(b)). Two constraints namely $\Phi_{TS}$ and $\Phi_{AI}$ restricted trigonum scapulae (TS) and angulus inferior (AI) respectively on the scapula medial boarder to glide over two ellipsoids approximating the thorax and the underlying soft tissues. The ISB recommendations (International Society of Biomechanics, 2005) were followed to define six bone-fixed frames. A generalized coordinate vector ($\boldsymbol{q} = [q_1 \ \ldots \ q_{11}]^T$) was considered to define the upper extremity configuration. The forward kinematic map ($\xi$) was developed to define the inertial coordinate of the $j^{th}$ bony landmark ($\boldsymbol{x}_j$) associated with the generalized coordinates at time $t$ (Appendix A.1).

### 2.2.2. Dynamic model

Mass and inertial properties were attributed to the bone segments according to Garner and Pandy (Garner and Pandy 2001). The upper extremity equations of motion were derived using the Lagrange's equations (Appendix A.2).

The origins/insertions, via points, and wrapping objects of 42 muscles spanning the upper extremity joints were defined from the MRI scans, including subclavius, serratus anterior upper/middle/lower, trapezius C1-C6/C7/T1/T2-T7, levator scapulae, rhomboid minor/major T1-T2/major T3-T4, pectoralis minor/major clavicular/major sternal/major ribs, latisimuss dorsi thoracic/lumbar/Iliac, deltoid clavicular/acromial/scapular, supraspinatus, infraspinatus, subscapularis, teres minor/major, coracobrachialis, triceps brachii long/medial/lateral, biceps brachii short/long, brachialis, brachioradialis, supinator, pronator Teres, flexor carpi radialis/ulnaris, and extensor carpi radiali long/radialis bervis/ulnaris (Ingram 2015). Each muscle group of the model can be represented by up to 20 strings (Figure 3). Three strings per muscle were considered for the simulations of this study.

## 2.3. Multi-segment optimization

The measured motion was reconstructed in terms of the generalized coordinates using multi-segment optimization. Given that GH was not a palpable bony landmark, it was missing from the measurements. Both TS and AI were also missing, because, TS and AI were masked with thick layers of soft tissues and were not effectively trackable (Matsui et al. 2006). Therefore, a novel method developed in (Sarshari 2018) was applied to estimate GH, TS, and AI trajectories, without requiring an additional scapula tracking device. Then, multi-segment optimization was used to define the generalized coordinates ($\boldsymbol{q}_i$) for each frame of the measured motions ($i$), such that the overall distance between the measured markers ($\boldsymbol{x}_{e_j}$) and their corresponding bony landmarks ($\boldsymbol{x}_{m_j}$) was minimized, while satisfying the forward kinematics map

$$\begin{aligned} \min_{\boldsymbol{q}_i} . \quad & \sum_j (\boldsymbol{x}_{m_{j,i}}(\boldsymbol{q}_i) - \boldsymbol{x}_{e_{j,i}})^T W (\boldsymbol{x}_{m_{j,i}}(\boldsymbol{q}_i) - \boldsymbol{x}_{e_{j,i}}) \\ \text{s.t.} \quad & \Phi_{TS}(\boldsymbol{q}_i) = 0 \\ & \Phi_{AI}(\boldsymbol{q}_i) = 0 \end{aligned} \tag{1}$$

where $W$ was a weighting matrix.

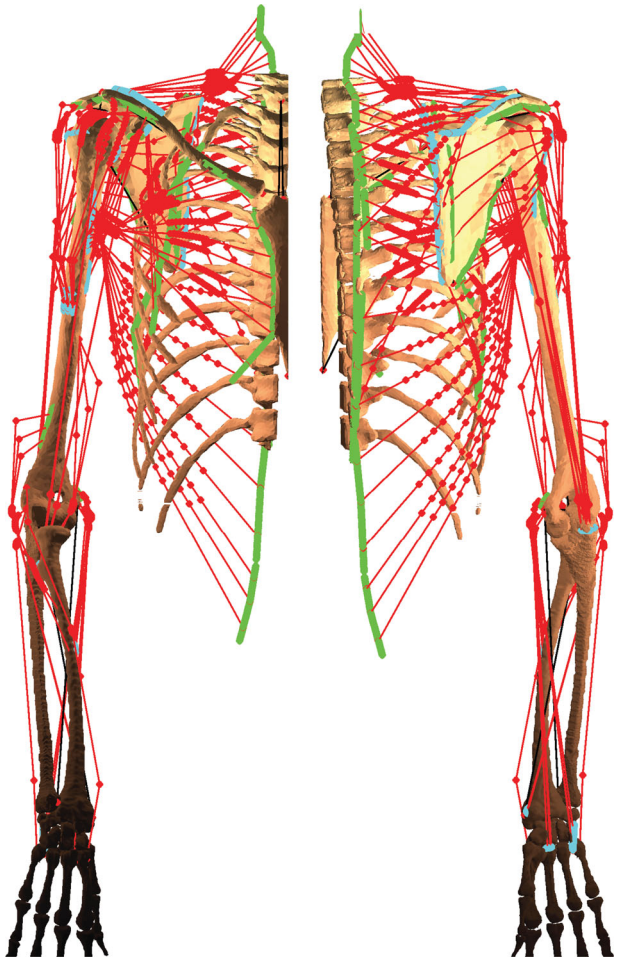

**Figure 3.** The developed shoulder and elbow musculoskeletal model included 42 muscles that each could be replicated by up to 20 strings (three strings were considered in this illustration).

### 2.4. Musculotendon model

A Hill-type musculotendon model was used to estimate the muscle forces associated with the measured EMG signals. It provided estimations of tendon force ($F_T(t)$) for given muscle excitations ($u(t)$) and muscuoltendon lengths ($l^{MT}(t)$) (Figure 4) (Winters and Stark 1987). It consisted of two unidirectional coupled dynamics, namely activation dynamics and contraction dynamics. The activation dynamics associated $u(t)$ to muscle activation ($a(t)$). The contraction dynamics accounted for the force reproductions for a given $a(t)$ and $l^{MT}(t)$ (Appendix A.3). A novel method developed in (Sarshari 2018) was used to solve the contraction dynamics so that the resulting tendon force estimations were devoid of artificial transients. In addition, the musculotendon model was validated by reproducing experimentally measured forces on maximally excited rat Soleus (Sarshari 2018).

### 2.5. EMG-assisted load-sharing (EALS)

The equations of motion (Equation (A.6)) provided eleven second order differential equations for the resulting generalized coordinates $\boldsymbol{q}$ obtained from the multi-segment optimization (Equation (1)). There were more unknowns (42 muscles times number of strings per muscle) than the number of equations. Therefore, we casted the following EALS to find an augmented muscle-force vector $\tilde{\boldsymbol{f}}_i \equiv [\boldsymbol{f}_i^T \ \lambda_{TS_i} \ \lambda_{AI_i}]^T$ for each frame of the measured motions $i$. As per Appendix A.2, $\boldsymbol{f}_i$ was a vector consisting of the magnitudes of all the muscle forces at $i$. The $\lambda_{TS}$ and $\lambda_{AI}$ were the Lagrange multipliers associated with the scapula-thorax constraints.

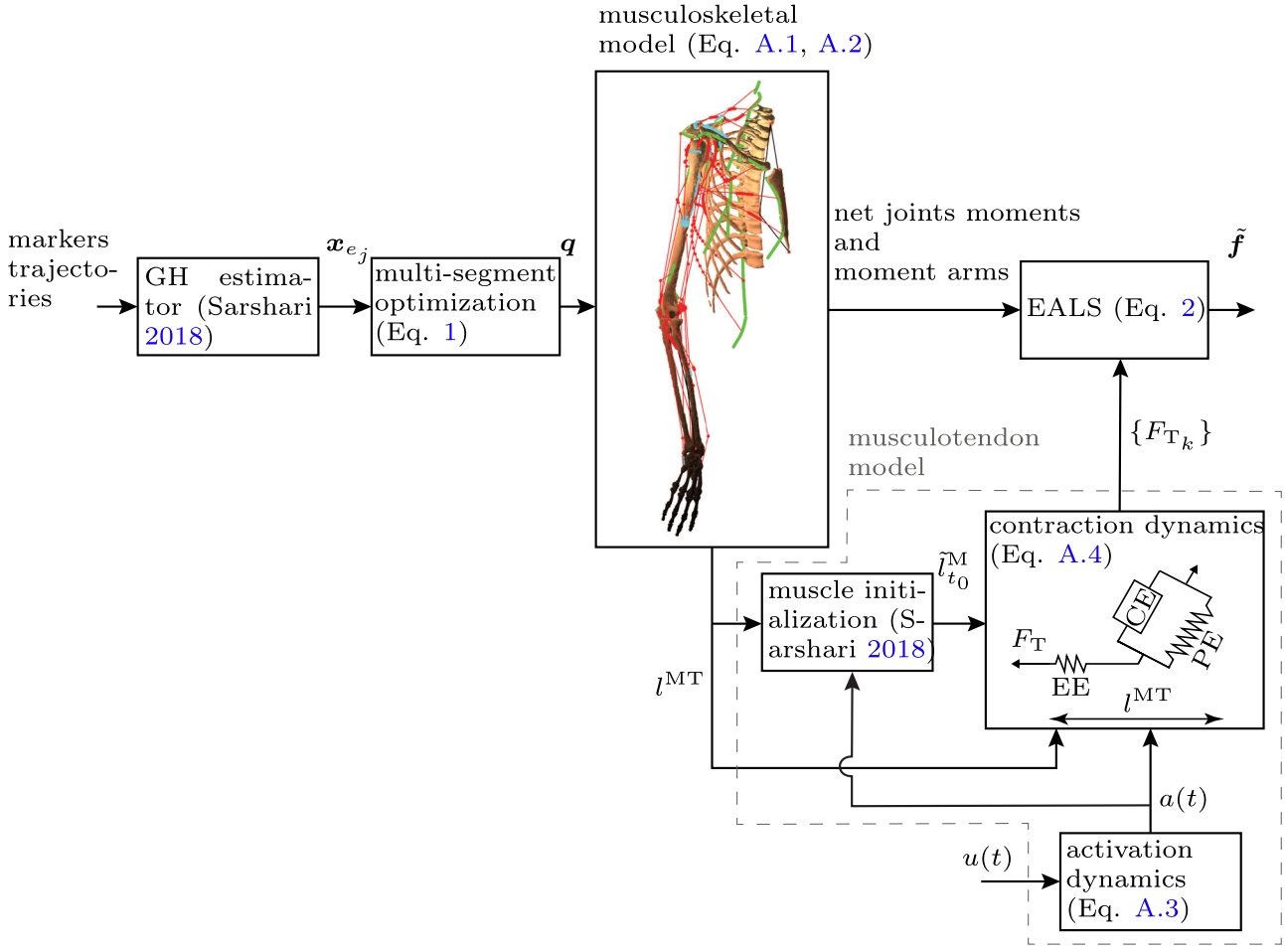


**Figure 4.** Markers trajectories were fed into the GH estimator. The resulting completed trajectories ($\boldsymbol{x}_{e_j}$) were used in the multi-segment optimization to find $\boldsymbol{q}$. The musculoskeletal model defined the net joints moments, moment arms, and $l^{MT}$. The muscle initialization provided $\tilde{l}^M_{t_0}$ for the contraction dynamics. The contraction dynamics reproduced the muscle forces associated to muscles with measured EMG ($\{F_{T_k} \ \forall k \in D_{EMG}\}$) for given $\tilde{l}^M_{t_0}$, $a(t)$, and $l^{MT}$. The resulting $F_{T_k}$ were used together with the net joints moments and moment arms in the EALS to estimate $\tilde{\boldsymbol{f}}$.

$$\begin{aligned}
&\min_{\tilde{f}_i} \quad \tilde{f}_i^T P \tilde{f}_i \\
&\text{s.t.} \quad \frac{d}{dt}\left(\frac{\partial \mathcal{L}}{\partial \dot{q}_i}\right) - \frac{\partial \mathcal{L}}{\partial q_i} = \left[\frac{\partial \Omega}{\partial \dot{q}_i} B \;\; \frac{\Phi_{TS}}{\partial q_i} \;\; \frac{\Phi_{AI}}{\partial q_i}\right] \tilde{f}_i \\
&\quad \begin{cases} (1-\epsilon) F_{T_{k,i}} \le \tilde{f}_k \le (1+\epsilon) F_{T_{k,i}} & k \in D_{EMG} \\ 0 \le \tilde{f}_k \le \tilde{f}_{max_k} & \text{else} \end{cases} \\
&\quad \psi(q_i, \dot{q}_i, \ddot{q}_i, \tilde{f}_i) \le 0
\end{aligned} \tag{2}$$

where $P$ was a diagonal matrix including the inverse squared of muscles physiological cross section areas (PCSA). The numerical values for PCSAs were set according to the same data set as for the musculotendon parameters (Garner and Pandy 2003). The cost function ($\tilde{f}_i^T P \tilde{f}_i$) was the sum of squared muscle stresses. The first set of constraints was the equations of motion (Equation (A.6)) whose right-hand side was written in a vectorial form. The second set of constraints was the muscle force upper/lower bounds. The set $D_{EMG}$ included muscles with measured EMG signals. If the $k^{th}$ muscle segment belonged to $D_{EMG}$, its tendon force estimated by the musculotendon model ($F_{T_{k,i}}$) from the measured EMG was used as its upper/lower bounds. The positive coefficient $\epsilon$ defined the portion of $F_{T_{k,i}}$ that was considered. The smallest $\epsilon$ that resulted in feasible solutions was considered for both activities (0.05 and 0.07 for flexion and abduction, respectively). For muscles without measured EMG signals, 0 and $\tilde{f}_{max_k} = K\ PCSA_k$ were used as their lower and upper bounds, respectively. The Fick constant $K$ was set to $33.011\,Nm^{-2}$ (Crowninshield and Brand 1981). The third constraint represented the stability constraint and denoted by $\psi$ (Ingram 2015). The stability constraint $\psi$ restricted the solution so that the resulting GH joint reaction force always pointed toward the inside of an elliptic cone that approximated the glenoid fossa. Mathematically, $\psi$ was defined as the scalar product between the normal vectors of the cone surface at the cone base and the GH joint reaction force

$$\begin{aligned}
&\psi = N.\left(\sum_k m_k(\ddot{x}_k - g) - Df\right) \le 0, \\
&k = \{\text{Humerus, Ulna, Radius}\}
\end{aligned} \tag{3}$$

where $N$ was the matrix containing the normal vectors, $m_k$ was the mass, $\ddot{x}$ is the linear acceleration of center of mass, $g$ was the gravitational acceleration, and $D$ was a matrix containing the muscle force direction vectors. We considered 40 normal vectors to adequately discretize the boundaries of the glenoid fossa, which resulted in 40 inequality constraints representing the stability constraint.

Equation (2) was solved to define $\tilde{f}$ such that the sum of squared muscle stresses was minimized, while the constraints were satisfied. The resulting $q$ from the multi-segment optimization was fed into the musculoskeletal model to obtain $l^{MT}$ for the full span of the measured motion. The musculotendon dynamics (Equations (A.7) and (A.8)) could be then solved upfront for the full span of the measured motion to define $F_{T_k}$. Having provided $F_{T_k}$, the net joints moments, and the moment arms with a given resolution, the optimization problem of Equation (2) was carried out separately for each frame of the measured motion ($i$). The equivalent SLS corresponds to $D_{EMG} = \{\}$.

### 2.6. Results analysis

The two measured activities were simulated using both SLS and EALS (Figure 4).

The stability ratio (SR) was defined for the glenohumeral joint based on the intersection of the JRF and an ellipse approximating the fossa (Equation (4)). It quantified the concentricity of the JRF with respect to the glenoid fossa. It is well-known that co-contractions increase the glenohumeral joint stability by centralizing the JRF within the fossa (Yanagawa et al. 2008). Therefore, the SR was linked to the GH joint stability obtained by co-contractions.

$$SR_i = 1 - \left(\frac{d_{IS_i}}{a_{IS}}\right)^2 - \left(\frac{d_{PA_i}}{a_{PA}}\right)^2 \tag{4}$$

where $a_{PA}$ and $a_{IS}$ were posterior-anterior and inferior-superior radii of an ellipse that approximates the glenoid fossa. $d_{PA_i}$ and $d_{IS_i}$ were intersections of JRF and the glenoid fossa ellipse in posterior-anterior and inferior-superior directions for the $i^{th}$ of the measured kinematics, respectively. The stability ratio lied within [01] with SR = 0 being marginal stability (intersection occurred on boundaries of the glenoid fossa ellipse), and SR = 1 being a perfectly centered intersection.

The sensitivities of the resulting muscle forces and JRF, with respect to $\pm 1\sigma_{EMG}$ variations of the normalized EMG signals around EMG means, were also defined. To this end, a first-order approximation (Fiacco 1976) of the sensitivity of Equation (2) with respect to $u(t)$ was calculated (Sarshari 2018).

Muscle forces, GH joint reaction force, and stability ratio were presented for the measured flexion and abduction. The sensitivities of the muscle forces and the JRF were also presented. The results were illustrated along the arm flexion and abduction angles corresponding to the flexion and abduction,

respectively. The associated results from the SLS were also presented. For the JRF, the corresponding *in vivo* measurements from (Bergmann et al. 2011) were also presented. Due to space limits, the complete set of muscle force estimations were left for the Appendix B and only a subset of them were presented.

## 3. Results

### 3.1. Muscle forces

#### 3.1.1. Forward flexion in the sagittal plane

While SLS estimated no force for deltoid clavicular and scapular (except between 60° to 80° flexion), EALS estimated forces (higher than 52 N) for the entire movement (Figure 5(a)). Deltoid acromial force followed similar patterns in EALS and SLS, but it was 30% higher initially in EALS. Deltoid acromial had the highest sensitivity (around 25%) to variations of the normalized EMG.

The supraspinatus and subscapularis forces were 390% and 90% higher in EALS than SLS, respectively. The infraspinatus and teres minor forces were similar in EALS and SLS (less than 10% difference in their maximums).

EALS estimated more than 50 N force for triceps long and biceps long (Figure B.1). However, SLS estimated only almost zero forces.

#### 3.1.2. Abduction in the fontal plane

EALS estimated above 55 N force for deltoid clavicular, whereas SLS estimated almost zero force (Figure 5(b)). Almost 145% higher force estimated by EALS for deltoid acromial in the beginning, although SLS estimation was 60% higher at the end of the motion. Both methods estimated very similar forces for deltoid scapular after 50° abduction (normalized root mean squared error $> 0.024$ and $p < 0.0001$). Deltoid acromial as well had the highest sensitivity to variations of the normalized EMG.

Higher maximum forces estimated by EALS for supraspinatus, infraspinatus, subscapularis, and teres minor comparing to SLS. For instance, the maximum subscapularis force was 22% higher in EALS.

EALS estimated above 90 N and 40 N forces for triceps long and biceps long, respectively (Figure B.2). However, SLS estimated zero forces.

### 3.2. JRF

The maximum JRF estimations by EALS were 58% and 46% higher comparing to SLS for both flexion and abduction motions, respectively (Figure 6(a) and Figure 6(b)). They were 172% and 167% of body weight (855 N) and occurred at 68° flexion and 98° abduction, respectively. The resulting JRFs had around 22% sensitivity to the variations of the normalized EMG signals.

### 3.3. SR and intersection foci

The SR was higher for EALS than SLS (more stable GH joint) and reached 0.87 (vs 0.56 for SLS) until the end of flexion (Figure 7(a)). The maximum SR was 46% less in abduction than in flexion according to EALS (Figure 7(b)).

## 4. Discussion

The aim of this study was to improve estimations of muscle co-contractions by simultaneously incorporating EMG data of fifteen muscles into a shoulder

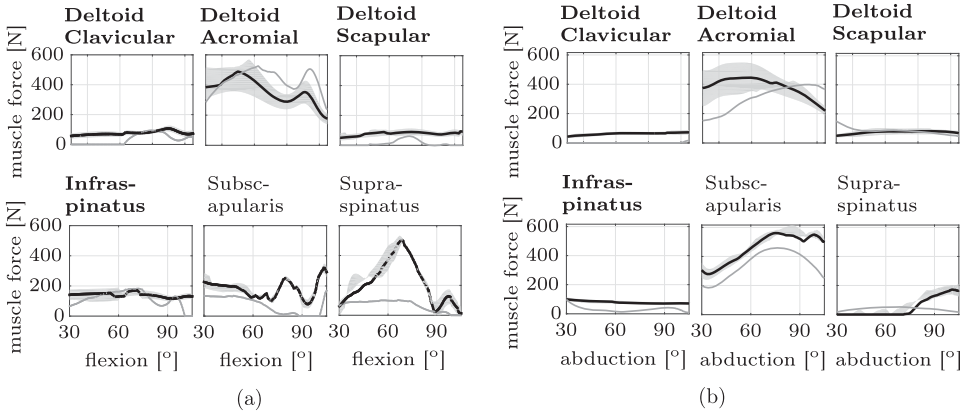


Figure 5. Muscle forces estimated by EALS (——) and SLS (——) for (a) flexion and (b) abduction with 2 kg weight in hand. The sensitivities to variations of normalized EMG signals were depicted by gray shaded areas. Bold fonts were used to distinguish the muscles with measured EMG data. The muscle force estimations for all the 42 muscles were presented in the Appendix B.

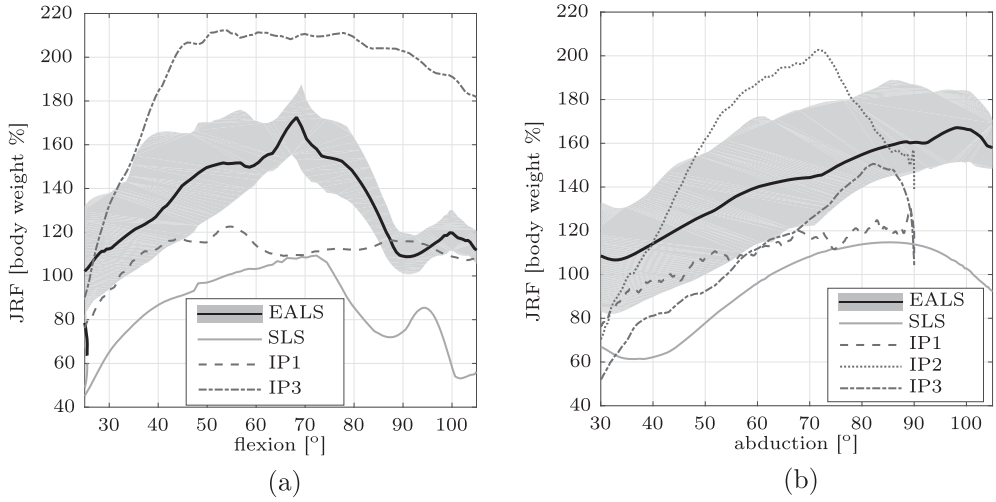


**Figure 6.** JRF estimated by EALS and SLS for (a) flexion, (b) abduction with 2 kg weight in hand along the corresponding *in vivo* measurements (IP1, IP2, and IP3) from (Bergmann et al. 2011). The sensitivities to variations of normalized EMG signals were depicted by the gray shaded areas.

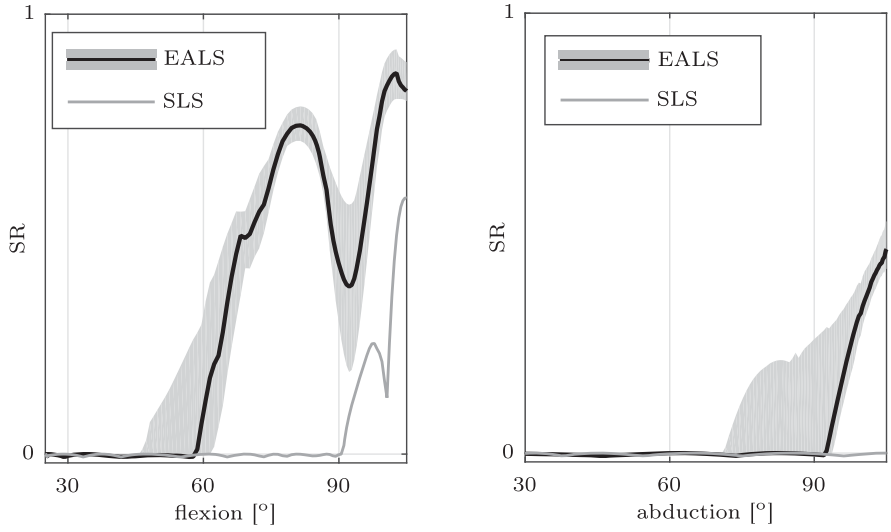


**Figure 7.** SR from EALS and SLS for (a) flexion and (b) abduction with 2 kg weight in hand. The sensitivities to variations of normalized EMG signals were also depicted by the gray shaded areas.

musculoskeletal model. To this end, the EALS was developed by modifying the SLS of a shoulder and elbow musculoskeletal model. The EALS was evaluated by comparing its muscles forces, JRF, and SR with those of the equivalent SLS. The developed EALS estimated higher muscle co-contractions compared to the SLS. The JRF was consequently higher compared to SLS.

During forward flexion, the higher force estimated for deltoid clavicular by EALS coincided with a higher force from deltoid scapular. This was consistent with the previous findings regarding the antagonistic role of deltoid scapular during arm flexion (Jost et al. 2000). Their co-contractions resulted in counterproductive moments around the GH joint. As well, higher forces were estimated for triceps long and biceps long as antagonistic muscles. Their antagonistic role for the GH joint movements was reported (Pagnani et al. 1996).

During abduction, similar co-contractions as those of flexion were estimated by EALS. Furthermore, pectoralis major sternal and teres major had higher forces in EALS, indicating their higher co-contractions. This co-contraction around the GH joint was consistent with previous studies (Steenbrink et al. 2009).

Comparison of the EALS and the SLS muscle force estimations also illustrated role exchanges among muscle groups with similar roles. For instance, trapezius and rhomboid muscles contributed in the scapular

upward/downward rotation during flexion. EALS estimated more contributions from rhomboid minor/major T1-T2 and less from trapezius C7/T2-T7. The SLS estimations were contrary. Indeed, the use of subject's EMG data in terms of upper/lower bounds in EALS caused these role exchanges. Therefore, this illustrated the potential of EALS in replicating inter-individual muscle recruitment patterns.

The JRF of EALS for both flexion and abduction activities lied within measurements from different patients with instrumented prosthesis (IP) (Bergmann et al. 2011). However, SLS in general underestimated the JRF in both activities. The IP measurements were averaged per activity among different patients with IP to draw a quantitative comparison between the JRF of EALS and SLS, and the IP measurements. Indeed, more patients with the IP measurements as well as more patients/activities simulated by the model were required for the comparison to be statistically relevant. Nevertheless, for flexion motion, the peak JRF was 3% higher for EALS and 34% lower for SLS compared to the peak JRF of the averaged IP1 and IP3 measurements. For abduction motion, the peak JRF was 12% higher for EALS and 24% lower for SLS compared to the peak JRF of the averaged IP1, IP2, and IP3 measurements. The JRF estimation from EALS was in general higher for the beginning of motions compared to the averaged IP measurements (23% and 69% higher for flexion and abduction, respectively). The trends of the estimated JRF by EALS were in general consistent with the IP measurements. It is worth noting that the IP measurements, as means of validation, should be used with caution. The post-surgery patients with IP had impaired musculotendons, and their motions were also compromised due to pain (Prinold et al. 2013). Therefore, their GH joint functions were expected to be different from our healthy subject.

The SR illustrated the effects of higher co-contractions of EALS on the GH joint stability. The higher co-contractions acted toward stabilizing the GH joint by centralizing the JRF within the glenoid ellipse. For the beginning of both activities, the SR was low, indicating that the GH joint stability constraint was active. This was consistent with the previous studies regarding stability of the GH joint (Veeger and Van Der Helm 2007; Yanagawa et al. 2008). In EALS, however, the SR started increasing at lower flexion and abduction angles.

In addition, the stability constraint could oscillate between active and inactive states, even for negligible deviations of JRF direction from the stability cone. This was due to the incorporation of the stability constraint as a hard constraint into EALS. A soft constraint formulation could, however, avoid these oscillatory behaviors without compromising the physiological correspondence of the stability constraint (Boyd and Vandenberghe 2004).

The positive coefficient $\epsilon$ was used to define the upper/lower bounds from EMG-based muscle forces in EALS. The choice of $\epsilon$, therefore, altered the optimal force estimation by changing the feasible set. Smaller values of $\epsilon$ further shrank the feasible set of the EALS compared with larger values of $\epsilon$. Consequently, higher co-contractions could be estimated. We considered the smallest $\epsilon$ that resulted in feasible solutions for both activities. This provided the highest estimations of muscle co-contractions using our model and allowed performing an adequately fare comparison between the force estimations of the two simulated activities. A sensitivity analysis could, however, quantify the effects of $\epsilon$ on the force estimations.

The number of muscle strings considered for each muscle also affected the optimal force estimation by changing the dimension (degrees of freedom) of the EALS. However, small effects were reported for the variations in muscle-string numbers (Van der Helm and Veenbaas 1991). We used three strings per muscle to adequately replicate muscles with large attachment sites.

A major limitation of this study was that only one subject was recorded. A larger number of subjects would be required for a more thorough model evaluation, specially, to evaluate its performance in replicating inter-individual muscle recruitment patterns. Three patients with instrumented prosthesis were considered finding the best combination of EMG signals during forward flexion and abduction (Nikooyan et al. 2012). The second limitation was about the musculotendon parameters. The realism of the reproduced forces could have been enhanced if these parameters were personalized to our subject. For the moment, it is not yet straightforward to obtain these parameters. The third limitation was that only two activities were considered. This imposed certain limitations to generalizing our results. Future applications of the model should consider more activities, including activities of daily living.

In conclusion, we verified the potential of EALS in better estimating muscle co-contractions in a shoulder and elbow musculoskeletal model compared with SLS. The EALS estimated co-contractions by incorporating fifteen EMG-based muscle forces obtained from a

musculotendon model. The incorporation of the EMG-based muscle forces shrank the feasible set of the EALS, and more co-contractions could therefore be estimated compared to the SLS. The JRF estimations better matched *in vivo* measurements, although EALS tended to overestimate JRF. This conclusion should be confirmed through simulations of more patients while patients perform more movements including activities of daily living.

## Disclosure statement

No potential conflict of interest was reported by the author(s).

## Acknowledgment

The authors thank Dr. Nicolas Place (Institute of Sports Sciences/Department of Physiology, Faculty of Biology and Medicine, UNIL) for providing the EMG measurement system.

## Funding

This project was supported by the Swiss National Science Foundation [143704].

## References

Arnold EM, Ward SR, Lieber RL, Delp SL. 2010. A model of the lower limb for analysis of human movement. Ann Biomed Eng. 38(2):269–279.

Baruh H. 1999. Analytical dynamics. Boston (MA): WCB/McGraw-Hill,

Bergmann G, Graichen F, Bender A, Rohlmann A, Halder A, Beier A, Westerhoff P. 2011. In vivo gleno-humeral joint loads during forward flexion and abduction. J Biomech. 44(8):1543–1552.

Boyd S, Vandenberghe L. 2004. Convex optimization. Cambridge, UK: Cambridge University Press.

Brookham RL, Middlebrook EE, Grewal T-j, Dickerson CR. 2011. The utility of an empirically derived co-activation ratio for muscle force prediction through optimization. J Biomech. 44(8):1582–1587.

Cholewicki J, McGill SM, Norman RW. 1995. Comparison of muscle forces and joint load from an optimization and emg assisted lumbar spine model: towards development of a hybrid approach. J Biomech. 28(3):321–331.

Collins J. 1995. The redundant nature of locomotor optimization laws. J Biomech. 28(3):251–267.

Crowninshield RD, Brand RA. 1981. A physiologically based criterion of muscle force prediction in locomotion. J Biomech. 14(11):793–801.

Dennerlein JT. 2005. Finger flexor tendon forces are a complex function of finger joint motions and fingertip forces. J Hand Ther. 18(2):120–127.

Engelhardt C, Malfroy Camine V, Ingram D, Müllhaupt P, Farron A, Pioletti D, Terrier A. 2015. Comparison of an emg-based and a stress-based method to predict shoulder muscle forces. Comput Methods Biomech Biomed Eng. 18(12):1272–1279.

Erdemir A, McLean S, Herzog W, van den Bogert AJ. 2007. Model-based estimation of muscle forces exerted during movements. Clin Biomech (Bristol, Avon)). 22(2):131–154.

Favre P, Sheikh R, Fucentese SF, Jacob HA. 2005. An algorithm for estimation of shoulder muscle forces for clinical use. Clin Biomech (Bristol, Avon)). 20(8):822–833.

Favre P, Snedeker JG, Gerber C. 2009. Numerical modelling of the shoulder for clinical applications. Philos Trans A Math Phys Eng Sci. 367(1895):2095–2118.

Fiacco AV. 1976. Sensitivity analysis for nonlinear programming using penalty methods. Math Program. 10(1):287–311.

Forster E, Simon U, Augat P, Claes L. 2004. Extension of a state-of-the-art optimization criterion to predict co-contraction. J Biomech. 37(4):577–581.

Gagnon D, Arjmand N, Plamondon A, Shirazi-Adl A, Larivière C. 2011. An improved multi-joint emg-assisted optimization approach to estimate joint and muscle forces in a musculoskeletal model of the lumbar spine. J Biomech. 44(8):1521–1529.

Garner BA, Pandy MG. 2000. The obstacle-set method for representing muscle paths in musculoskeletal models. Comput Methods Biomech Biomed Eng. 3(1):1–30.

Garner BA, Pandy MG. 2001. Musculoskeletal model of the upper limb based on the visible human male dataset. Comput Methods Biomech Biomed Engin. 4(2):93–126.

Garner BA, Pandy MG. 2003. Estimation of musculotendon properties in the human upper limb. Ann Biomed Eng. 31(2):207–220.

Herzog W. 1996. Force-sharing among synergistic muscles: theoretical considerations and experimental approaches. Exerc Sport Sci Rev. 24(1):173–202.

Hug F. 2011. Can muscle coordination be precisely studied by surface electromyography. J Electromyogr Kinesiol. 21(1):1–12.

Ingram D, Engelhardt C, Farron A, Terrier A, Müllhaupt P. 2016. Modelling of the human shoulder as a parallel mechanism without constraints. Mech Mach Theory. 100:120–137.

Ingram D. 2015. Musculoskeletal model of the human shoulder for joint force estimation. Ph.D. Thesis, Ecole Polytechnique Fédérale de Lausanne. doi:10.5075/epfl-thesis-6497.

Jost B, Pfirrmann CW, Gerber C. 2000. Clinical outcome after structural failure of rotator cuff repairs. JBJS. 82(3):304–314.

Labriola JE, Lee TQ, Debski RE, McMahon PJ. 2005. Stability and instability of the glenohumeral joint: the role of shoulder muscles. J Shoulder Elbow Surg. 14(1):S32–S38.

Langenderfer J, LaScalza S, Mell A, Carpenter JE, Kuhn JE, Hughes RE. 2005. An emg-driven model of the upper extremity and estimation of long head biceps force. Comput Biol Med. 35(1):25–39.

Laursen B, Jensen BR, Németh G, Sjøgaard G. 1998. A model predicting individual shoulder muscle forces based

on relationship between electromyographic and 3d external forces in static position. J Biomech. 31(8):731–739.
Matsui K, Shimada K, Andrew PD. 2006. Deviation of skin marker from bone target during movement of the scapula. J Orthop Sci. 11(2):180–184.
Nikooyan A, Veeger H, Westerhoff P, Bolsterlee B, Graichen F, Bergmann G, Van der Helm F. 2012. An emg-driven musculoskeletal model of the shoulder. Human Movement Sci. 31(2):429–447.
Pagnani MJ, Deng X-H, Warren RF, Torzilli PA, O'Brien SJ. 1996. Role of the long head of the biceps brachii in glenohumeral stability: a biomechanical study in cadavera. Journal of Shoulder and Elbow Surgery. 5(4): 255–262.
Prinold JA, Masjedi M, Johnson GR, Bull AM. 2013. Musculoskeletal shoulder models: a technical review and proposals for research foci. Proc Inst Mech Eng H. 227(10):1041–1057.
Raikova R. 1999. About weight factors in the non-linear objective functions used for solving indeterminate problems in biomechanics. J Biomech. 32(7):689–694.
Sarshari E, Farron A, Terrier A, Pioletti D, Mullhaupt P. 2017. A simulation framework for humeral head translations. Med Eng Phys. 49:140–147.
Sarshari E. 2018. A closed-loop EMG-assisted shoulder model. Ph.D. Thesis, Ecole Polytechnique Fédérale de Lausanne. doi:10.5075/epfl-thesis-8658.
Siciliano B, Khatib O. 2008. Springer handbook of robotics. Berlin: Springer-Verlag, ISBN: 978-3-540-23957-4.
Steenbrink F, De Groot J, Veeger H, van der Helm F, Rozing P. 2009. Glenohumeral stability in simulated rotator cuff tears. J Biomech. 42(11):1740–1745.
Terrier A, Aeberhard M, Michellod Y, Mullhaupt P, Gillet D, Farron A, Pioletti DP. 2010. A musculoskeletal shoulder model based on pseudo-inverse and null-space optimization. Med Eng Phys. 32(9):1050–1056.
Van der Helm FC, Veenbaas R. 1991. Modelling the mechanical effect of muscles with large attachment sites: application to the shoulder mechanism. J Biomech. 24(12): 1151–1163.
Van der Helm FC. 1994. Analysis of the kinematic and dynamic behavior of the shoulder mechanism. J Biomech. 27(5):527–550.
Veeger H, Van Der Helm F. 2007. Shoulder function: the perfect compromise between mobility and stability. J Biomech. 40(10):2119–2129.
Winter DA. 2009. Biomechanics and motor control of human movement. John Wiley & Sons.
Winters JM, Stark L. 1987. Muscle models: what is gained and what is lost by varying model complexity. Biol Cybern. 55(6):403–420.
Wu G, Van der Helm FC, Veeger HD, Makhsous M, Van Roy P, Anglin C, Nagels J, Karduna AR, McQuade K, Wang X, International Society of Biomechanics, et al. 2005. Isb recommendation on definitions of joint coordinate systems of various joints for the reporting of human joint motion-Part II: shoulder, elbow, wrist and hand. J Biomech. 38(5):981–992.
Yanagawa T, Goodwin CJ, Shelburne KB, Giphart JE, Torry MR, Pandy MG. 2008. Contributions of the individual muscles of the shoulder to glenohumeral joint stability during abduction. J Biomech Eng. 130(2):021024
Zajac FE. 1989. Muscle and tendon properties models scaling and application to biomechanics and motor. Crit Rev Biomed Eng. 17(4):359–411.

## Appendix A. Mathematical representations

### A.1. Forward kinematic map ($\xi$)

The forward kinematic map ($\xi$) defined the inertial coordinate of the $j^{\text{th}}$ bony landmark ($\boldsymbol{x}_j$) associated with the generalized coordinates at time $t$.

$$\begin{aligned}
&\xi : C_s \subset R^{11} \mapsto W_s \subset R^3 \\
&\xi(\boldsymbol{q}(t)) \;\; = \boldsymbol{x}_j(t), \quad j = \{\text{C7}, \;\ldots,\; \text{RS}\}_{1\times 14} \\
&\Phi_{\text{TS}}(\boldsymbol{q}(t)) = ({}_t\boldsymbol{TS}(t) - {}_t\boldsymbol{e}_0)^T E_{\text{TS}} ({}_t\boldsymbol{TS}(t) - {}_t\boldsymbol{e}_0) - 1 = 0 \\
&\Phi_{\text{AI}}(\boldsymbol{q}(t)) = ({}_t\boldsymbol{AI}(t) - {}_t\boldsymbol{e}_0)^T E_{\text{AI}} ({}_t\boldsymbol{AI}(t) - {}_t\boldsymbol{e}_0) - 1 = 0
\end{aligned} \tag{A.1}$$

where $C_s$ and $W_s$ were the coordinate space and work space of the model (Siciliano and Khatib 2008). Two holonomic constraints ($\Phi_{\text{TS}} = 0$ and $\Phi_{\text{AI}} = 0$) replicated the kinematic relationships between the scapula and the thorax (scapulothoracic contact). The left-hand side subscript $t$ specified that the landmarks were in the thorax (inertial) frame. The ellipsoids center was ${}_t\boldsymbol{e}_0$, and $E_{\text{TS}}$ and $E_{\text{AI}}$ were the ellipsoids matrices. The use of two separate ellipsoids to replicate the scapulothoracic contact reduced the computational complexity of $\xi$ (Ingram 2015) comparing to the previous models where only one ellipsoid was used (Van der Helm 1994; Garner and Pandy 2001; Nikooyan et al. 2012). The use of one ellipsoid required computing the projections of the TS and AI onto the ellipsoid.

### A.2. Equations of motion

The upper extremity equations of motion were derived using the Lagrange's equations (Equation (A.2)).

$$\frac{d}{dt}\left(\frac{\partial \mathcal{L}}{\partial \dot{\boldsymbol{q}}}\right) - \frac{\partial \mathcal{L}}{\partial \boldsymbol{q}} = \frac{\partial \Omega}{\partial \dot{\boldsymbol{q}}} M + \lambda_{\text{TS}} \frac{\Phi_{\text{TS}}}{\partial \boldsymbol{q}} + \lambda_{\text{AI}} \frac{\Phi_{\text{AI}}}{\partial \boldsymbol{q}} \tag{A.2}$$

where $\mathcal{L}$ was the Lagrangian of the model obtained by adding all the bone segments Lagrangians (Ingram 2015; Sarshari 2018). The $\frac{\partial \Omega}{\partial \dot{\boldsymbol{q}}} M$ was the generalized force vector. The $\Omega$ was a horizontal matrix including the angular velocities of all the bone segments. The vertical matrix $M$ consisted of the muscle resultant moments around each one of the five joints. The $\lambda_{\text{TS}}$ and $\lambda_{\text{AI}}$ were Lagrange multipliers associated with the scapula-thorax constraints. The generalized moment arms of the constraints were obtained by their Jacobians ($\frac{\Phi_{\text{TS}}}{\partial \boldsymbol{q}}$ and $\frac{\Phi_{\text{AI}}}{\partial \boldsymbol{q}}$) (Baruh 1999).

The matrix $M$ was written as $M = B\boldsymbol{f}$, where $B$ was the moment arm matrix, and $\boldsymbol{f}$ was a vector consisting of the magnitudes of all the muscle forces. The $B$ was obtained using its geometric definition based on the obstacle set method (Garner and Pandy 2000).

### A.3. Musculotendon model

The means of normalized EMG signals were used as $u(t)$ for each muscle. The $a(t)$ represented the relative amount of calcium release to troponin in muscle fibers. It was obtained from a first order dynamic as follows (Zajac 1989).

$$\frac{da(t)}{dt} = \frac{u(t)-a(t)}{\tau(a(t),u(t))},$$
$$\tau(a(t),u(t)) = \begin{cases} \frac{\tau_{act}}{0.5+1.5a(t)} & u(t) \le a(t) \\ \frac{\tau_{dact}}{0.5+1.5a(t)} & u(t) > a(t) \end{cases} \quad (A.3)$$

where $\tau_{act}$ and $\tau_{dact}$ were time constants corresponding to muscle activation and deactivation, respectively. Both $u(t)$ and $a(t)$ lied within [01].

The contraction dynamics consisted of three elements replicating the force production of the musculotendon, including a contractile element (CE), a passive elastic element (PE), and an elastic element (EE) (Zajac 1989). The contraction dynamics were derived from a force equilibrium between the muscle fiber and tendon. The following ordinary differential equation was an implicit form of the contraction dynamics (Sarshari 2018)

$$F_O\left[a(t)f^L(\tilde{l}^M)f^V\left(\frac{l_O^M}{v_O^M}\dot{\tilde{l}}^M\right)+f^P(\tilde{l}^M)\right]\sqrt{1-\left(\frac{\sin\alpha_O}{\tilde{l}^M}\right)^2} = F_O f^T\left(\frac{l^{MT}-l_O^M\sqrt{\tilde{l}^{M^2}-\sin\alpha_O{}^2}}{l_S^T}\right) \quad (A.4)$$

where $f^L(.), f^V(.), f^P(.)$, and $f^T(.)$ were normalized functions associated with muscle force-length, muscle force-velocity, muscle passive force, and tendon force-length relationships. The normalized functions were obtained by fitting smooth curves ($C^\infty$) to experimental data (Sarshari 2018). The maximum (optimum) muscle fiber force was denoted by $F_O$. The normalized muscle fiber length ($\tilde{l}^M$) was obtained as $\frac{l^M}{l_O^M}$ in which $l^M$ and $l_O^M$ were the muscle fiber length and its optimum, respectively. The optimum muscle fiber velocity and the tendon slack length were denoted by $v_O^M$ and $l_S^T$, respectively. The $l_O^M$ and $v_O^M$ corresponded to the situations when the muscle force-length and muscle force-velocity relationships were at maximum and zero force, respectively. Also, $\alpha_O$ is the pennation angle at $l_O^M$.

Equation (A.4) could be solved for $\tilde{l}^M$ to consequently provide the tendon force $F_T(t) = F_O f^T(.)$. To this end, $a(t)$, $l^{MT}(t)$, the five musculotendon parameters ($F_O, l_O^M, v_O^M, l_S^T$, and $\alpha_O$), and an initial condition $\tilde{l}^M(t_0)$ were required. The $a(t)$ was readily obtained from Equation (A.3). The $l^{MT}(t)$ was calculated for each muscle using the musculoskeletal model. More specifically, the resulting $\boldsymbol{q}$ from the multi-segment optimization was fed into the model. The model defined the paths and, consequently, the lengths of musculotendons. We set the five musculotendon parameters according to (Garner and Pandy 2003).

## Appendix B. Muscle forces

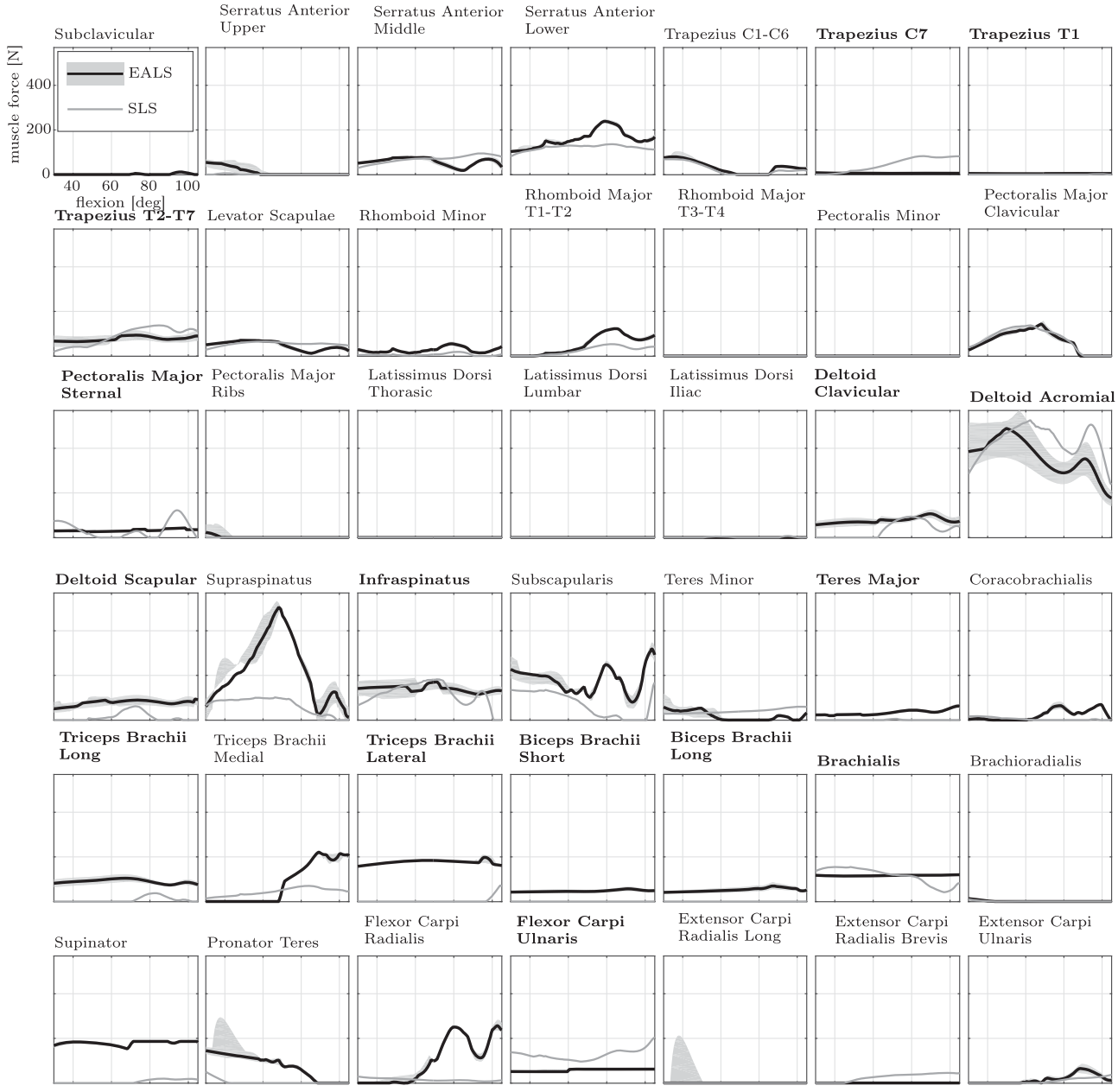


**Figure B1:** Muscle forces estimated by EALS and SLS for flexion. The sensitivities to variations of normalized EMG signals were also depicted by the gray shaded areas. Bold fonts were used to distinguish the muscles with measured EMG data.

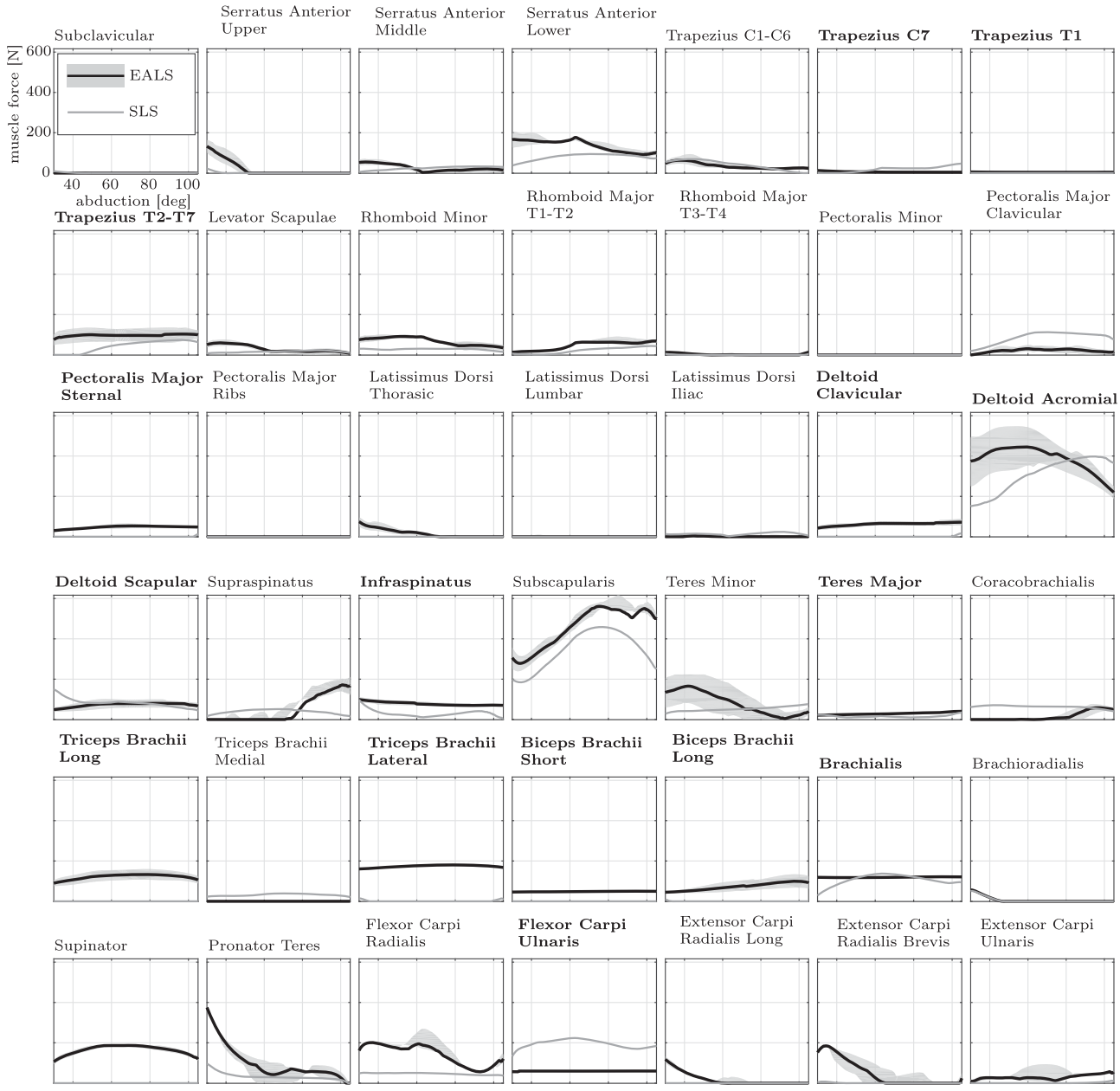


**Figure B2:** Muscle forces estimated by EALS and SLS for abduction. The sensitivities to variations of normalized EMG signals were also depicted by the gray shaded areas. Bold fonts were used to distinguish the muscles with measured EMG data.